Optimized single-shot laser ablation of concave mirror templates on optical fibers

THIBAUD RUELLE, MARTINO POGGIO, AND FLORIS BRAAKMAN*

Department of Physics, University of Basel, Klingelbergstrasse 82, 4056 Basel, Switzerland
*Corresponding author: floris.braakman@unibas.ch

We realize mirror templates on the tips of optical fibers using a single-shot CO_2 laser ablation procedure and perform a systematic study of the influence of the pulse power, pulse duration, and laser spot size on their geometry. This investigation provides new insights into CO_2 laser ablation of optical fibers and should help improve current models. We notably find that the radius of curvature, depth, and diameter of the templates exhibit extrema as a function of the power and duration of the ablation pulse, and observe that compound convex–concave shapes can be obtained. We additionally identify regimes of ablation parameters that lead to mirror templates with favorable geometries for use in cavity quantum electrodynamics and optomechanics. © 2019 Optical Society of America

1. INTRODUCTION

In the last decade, CO_2 laser ablation has become a mature technique for the processing of optical glasses, uniquely suited to fabricating micrometer-scale structures with sub-nanometer surface roughness [1,2]. A wide range of shapes can be produced using this technique, including microspheres [3], microlenses [4,5], microtoroids [6], gratings [1], holographic structures [7], and concave mirror templates [8,9]. In particular, concave mirror templates can be realized on the tips of optical fibers [8] and can be used to define tunable open-access Fabry–Perot microcavities [10,11]. The combination of spectral tunability, high finesse, intrinsic fiber coupling, and the uniquely small dimensions offered by these optical cavities has led to their widespread adoption in cavity quantum electrodynamics (CQED) [12–19], and to a lesser extent in optomechanics [20–23].

The main focus over the past few years has been developing multi-shot ablation procedures in order to improve control over the geometry of the concave shape [24–27]. These studies, alongside refined analytical and numerical cavity models [28–32], contributed to recent breakthroughs in trapped ion CQED [33], trapped atom CQED [34], solid-state QED [35], and optomechanics [36]. Nevertheless, few systematic studies of the effects of fabrication parameters on the geometry of structures created on the tip of an optical fiber by a single ablation pulse have been performed.

In this work, we focus on single-shot ablation, adding to the pioneering work from [8]. We realize mirror templates on the tips of a large number of optical fibers using varying pulse powers (0.5–3 W), pulse durations (10–50 ms), and spot sizes

(32–67 μm). We characterize in detail the influence of each of those three ablation parameters on the shape of the resulting structures, and more specifically on their radius of curvature, depth, and diameter. We then study the relationships between those three geometrical characteristics and identify regimes of ablation parameters that lead to templates with favorable geometries for use in CQED and optomechanics.

2. SETUP AND METHODS

Our CO_2 laser ablation setup is depicted in Fig. 1(a). Similar to the setup introduced in [25], it comprises both a CO_2 ablation arm and an imaging arm. An RF-pumped Synrad Firestar V30 10.6 μm CO_2 laser is driven by a 20 kHz pulse-width-modulated control signal using the dedicated UC-2000 controller. These conditions ensure a nearly continuous output and determine the maximum power that can be used for ablation. Here we use a 50% duty cycle, which corresponds to a maximum power of 2.1 W. The ablation pulses are shaped by imprinting a square temporal profile on the nearly continuous-wave CO_2 laser beam using a Brimrose GEM-40 acousto-optic modulator (AOM), to which we send square pulses of amplitude V_{AOM} between 0 V and 1 V and of duration τ ranging from 10 ms to 50 ms. In order to provide optical isolation, the beam goes through a Brewster polarizer and a quarter-wave plate. This also serves to make the beam circularly polarized, which reduces the ellipticity of ablated structures [32]. The beam is then expanded before being focused by a 50 mm focal length ZnSe aspheric lens. A mirror can be placed before the focusing lens in order to measure the incident power with a power meter, providing a mapping between the amplitude
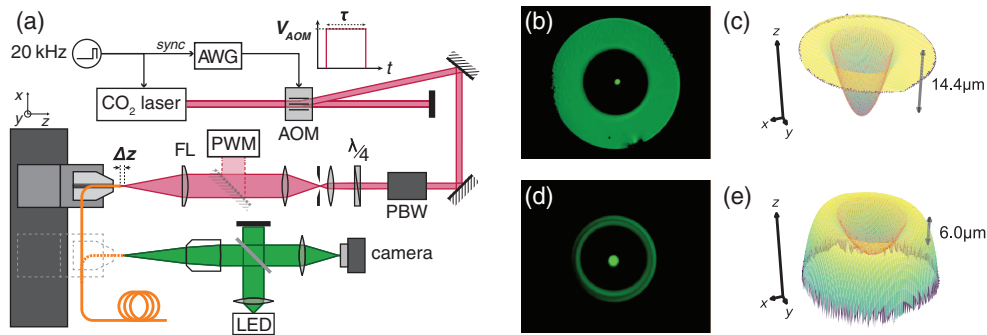
Fig. 1. (a) CO_2 ablation setup. AWG, arbitrary waveform generator; AOM, acousto-optic modulator; PBW, Brewster polarizer; PWM, power meter; FL, aspheric lens; Δz, distance between the focal point of the focusing lens and the ablation target. The inset shows the electronic pulse of amplitude V_{AOM} and duration τ that is sent to the AOM to shape the CO_2 ablation pulse. (b), (d) Microscope images of two different fibers after ablation. Only surfaces close to perpendicular to the illumination beam appear. (c), (e) Corresponding height profiles, measured by confocal laser profilometry. The red wireframe is obtained by fitting an elliptic paraboloid to the concave structure.

V_{AOM} of the pulse sent to the AOM and the power P_{CO_2} of the ablation pulse. The radius of the beam at the position of the target is controlled by positioning the target at a distance Δz from the focal point of the lens, ranging from 0 mm to –1 mm. The mapping between the defocusing distance Δz and the $1/e^2$ beam radius (spot size) w is calibrated by performing a series of knife-edge measurements of the beam profile for different values of Δz.

We use Thorlabs 780HP single-mode fibers, whose core and cladding diameters are 4.4 μm and 125 μm, respectively. Before ablation, each fiber is cut to length, stripped, cleaved using a Photon Kinetics PK11 ultrasonic cleaver, and positioned into a holder with about 2 mm of freestanding length.

The ablation procedure is then the following: (1) center the core of the fiber at the focal point of the imaging arm. The core appears as a bright spot on the microscope image due to the illumination light coupling into it and being reflected from the other end of the fiber. (2) Translate the holder by a calibrated distance so that the core of the fiber is located at the focal point of the CO_2 laser beam. (3) Tune the spot size at the position of the fiber by performing an additional displacement along the beam axis. (4) Trigger the ablation pulse. (5) Translate the holder back to the imaging arm to confirm centering and to roughly estimate the geometrical characteristics of the resulting structure [Figs. 1(b) and 1(d)].

Next, the height profiles of the ablated fibers are measured with a Keyence VK-X200K laser scanning confocal microscope with a vertical resolution of 0.5 nm and a lateral pixel size of 46.5 nm. Two examples of such profiles are shown in Figs. 1(c) and 1(e). We performed AFM measurements on a few of the fibers and found that the roughness at the center of the ablated structures is typically smaller than 0.3 nm rms, in good agreement with previously reported values [8].

For height profiles exhibiting a concave part, we extract their characteristic dimensions (see Fig. 2). We first correct for plane tilt, find the center of the structure, and calculate its outer diameter D_{out}, which we define as the diameter of the contour line at 5% of the depth of the structure. We then fit an elliptic paraboloid to the height profile cropped to a disk centered on the structure and whose radius is half the waist of a Gaussian fitted to a linecut through the structure. Next, we use the fit results to calculate the depth t of the structure and its radius of curvature $\mathrm{ROC} = (\mathrm{ROC}_a + \mathrm{ROC}_b)/2$, where ROC_a and ROC_b are the radii of curvature along the major and minor axes of the elliptic paraboloid, respectively. Finally, we evaluate the residuals of the fit and calculate the spherical diameter D_{sph} of the structure, which we define as the diameter of the disk centered on the structure for which fit residuals are smaller than 100 nm. D_{sph} is intended to be an estimate of the effective mirror diameter as used in [10].
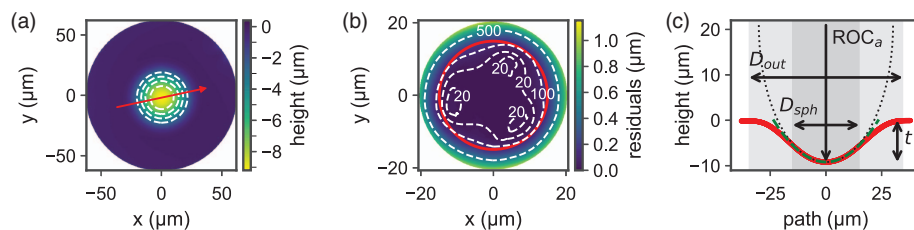

Fig. 2. Graphical output of the fitting routine. (a) Height profile of a fiber as measured by laser scanning confocal microscopy, all dimensions given in μm. The white dashed lines are contour lines at –7.6 μm, –6.1 μm, –4.5 μm, and –2.9 μm starting from the center. (b) Residuals of the fit of an elliptic paraboloid to the height profile in (a), with white dashed contour lines. The red circle shows the disk of diameter D_{sph} within which we consider the structure to be equivalent to a sphere of radius ROC. (c) Linecut through the height profile [red arrow in (a)]. The green dashed curve is the corresponding linecut through the best-fit elliptic paraboloid. The dotted black curve is the circle of radius ROC_a.

3. EFFECTS OF ABLATION PARAMETERS ON STRUCTURE SHAPE

CO_2 laser ablation is a complex, multi-physical process in which the dynamics of heat transfer, phase transitions, and liquid flow all come into play. The dominant phenomena for determining the shape created at the ablation site are strongly material dependent and change even for small variations in ablation parameters [37]. For instance, when the surface temperature is not raised above the vaporization temperature, material removal is minimal, and the ablation site undergoes mainly smoothing [38]. When vaporization occurs, for certain ablation parameters, a combination of vaporization and of melt displacement driven by recoil pressure can result in the formation of a concave shape [39]. Finally, if solidification occurs slowly enough, capillary forces can make the geometry evolve further, eventually leading to a convex shape [40]. Due mainly to a lack of quantitative understanding of the interplay between those phenomena during the ablation process and to a lack of data on material properties at high temperature, models have yet to demonstrate the ability to accurately predict the shape resulting from CO_2 laser ablation within an experimentally relevant range of ablation parameters [37,40–42]. Modeling is especially problematic for optical fibers, since radial boundary effects come into play [8]. This motivates us to study in detail the specific effect of each ablation parameter, aiming to extend the range of geometries that can be achieved and to provide guidelines for the fabrication of mirror templates for open micro-cavities.

We characterize the geometry of 129 structures formed on fiber facets following the single-shot CO_2 ablation procedure described above. We use pulse durations τ of 10 ms, 30 ms, and 50 ms and defocusing distances Δz of 0 mm, –0.1 mm, –0.2 mm, –0.3 mm, and –0.4 mm, corresponding to spot sizes w of 32 µm, 36 µm, 45 µm, 56 µm, and 67 µm. For each combination of those parameters, we perform a series of ablations with varying pulse power P_{CO_2}. We then measure the height profile of the fiber facets, which can be flat, concave, convex, or a mixture of convex and concave. For the 123 fibers that are concave in their centers, we fit this concave part to extract the geometrical characteristics of the structure.

In order to illustrate the effect of ablation pulse power on the shape, linecuts through the height profiles of a selection of fibers are plotted in Fig. 3(a). We distinguish phenomenologically five different regimes of pulse power, each of them leading to a different type of modification of the surface of the fiber,

some of which might not be observed depending on the value of the other ablation parameters. (1) For very low pulse powers, no modification of the surface occurs. (2) For low pulse powers, the overall geometry is not modified, but the area exposed to the laser is smoothed. (3) For medium pulse powers, concave structures are created, whose depth and outer diameter increase with pulse power. (4) For high pulse powers, concave structures whose depth and outer diameter decrease with pulse power are created within an increasingly convex shape. Such a shape prevents cleaving imperfections from limiting the minimum length of optical cavities, and previously required additional processing steps [43]. (5) For very high pulse power, a fully convex shape is created. The change from a concave to convex–concave geometry associated with the transition from regime 3 to regime 4 is highlighted in Fig. 3(b), where we plot the curvature of a convex parabola fitted to the outer part of the fibers whose linecuts are shown in Fig. 3(a). We now focus on the concave structures that are obtained in regimes 3 and 4, and discuss the effects of pulse power, pulse duration, and spot size on their geometry.

The geometrical characteristics ROC, t, D_{out}, and D_{sph} obtained by fitting the profiles of the fibers exhibiting concave structures are plotted in Fig. 4 as a function of the ablation parameters P_{CO_2}, τ, and w. In the low-power regime (regime 3), an increase in pulse power leads to a decrease in ROC, and an increase in depth, outer diameter, and spherical diameter. In the high-power regime (regime 4), an increase in pulse power leads to an increase in ROC, a decrease in depth and outer diameter, and an increase in spherical diameter. In both power regimes, an increase in spot size leads to an increase in ROC, a decrease in depth, and has no significant effect on the outer and spherical diameters. Increasing the pulse duration has a more complex effect: it generally shifts values of the geometrical characteristics to lower pulse powers and narrows their distribution. This results in a decrease in the pulse power corresponding to the onset of regime 4, associated with an increase in the sensitivity of the geometry to changes in pulse power. As a consequence, shorter pulse durations give finer control over the geometry of the structures, since deviations in pulse power have a smaller effect. In addition, decreasing the pulse duration decreases the minimum achievable ROC, increases the maximum achievable depth, and decreases the minimum achievable outer and spherical diameters. Note that we do not observe the defocusing distance to have a significant effect on crater asymmetry, which we measure to be 5% on average.
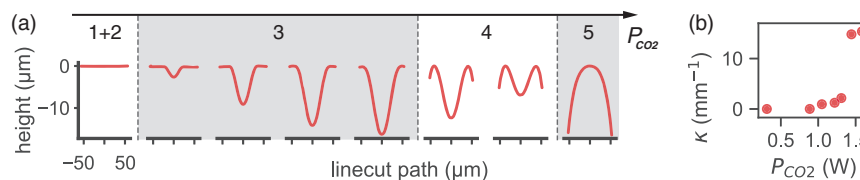

Fig. 3. (a) Linecuts taken through the measured height profiles of fibers ablated with increasing pulse power. The axis shows the direction along which P_{CO_2} increases and illustrates the power regimes defined in the main text. The values of P_{CO_2} used were 0.3 W, 0.9 W, 1.0 W, 1.2 W, 1.3 W, 1.4 W, 1.6 W, and 0.5 W for fibers from left to right. A spot size of 45 µm was used for all fibers. A pulse duration of 30 ms was used for all fibers but the rightmost, which was subjected to a 300 ms ablation pulse. (b) Plot as a function of P_{CO_2} of the curvature κ of a convex parabola fitted to the outer part of the fibers whose linecuts are shown in (a) and for which a pulse duration of 30 ms was used.
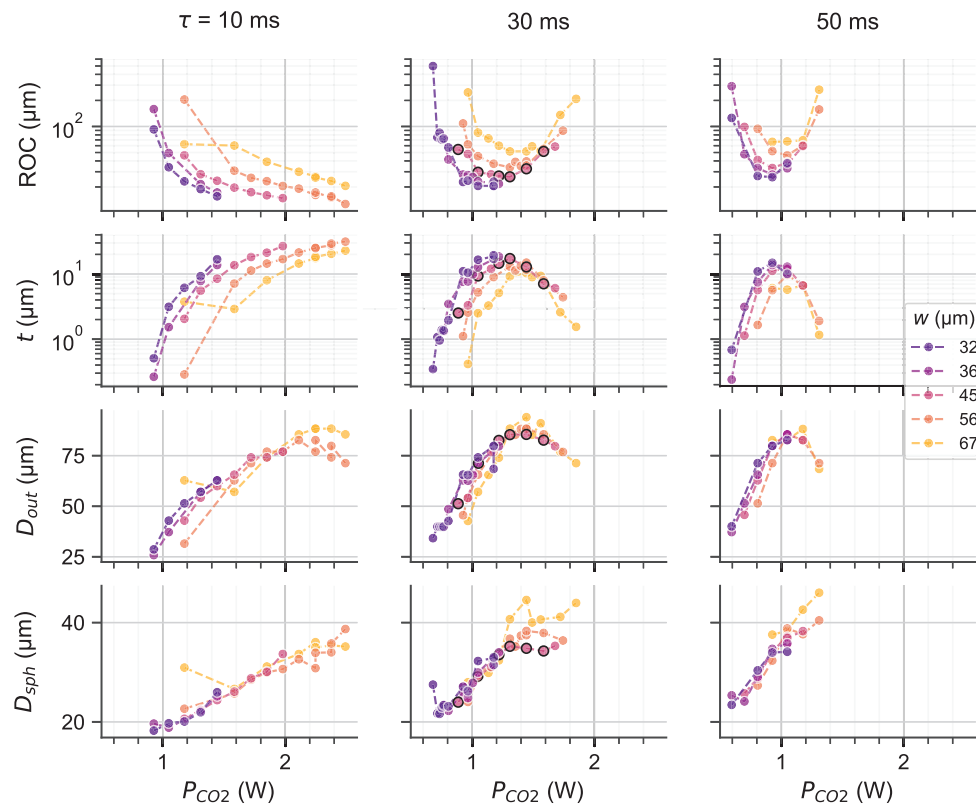
Fig. 4. Geometrical characteristics of ablated concave structures plotted as a function of ablation parameters. The different rows show plots of ROC, t, D_{out}, and D_{sph} as a function of the pulse power P_{CO_2}. The pulse duration τ is varied across columns, and the spot size w is encoded in the color of the points. Points corresponding to the fibers belonging to regimes 3 and 4, shown in Fig. 3(a), are outlined in black.

4. RELATIONSHIPS BETWEEN THE GEOMETRICAL CHARACTERISTICS OF CONCAVE STRUCTURES

Fiber-based Fabry–Perot optical microcavities are widely used in the fields of CQED [12–19,33,34] and optomechanics [20–23], with additional applications in sensing [44–46]. For most of these applications, it is desirable to minimize the waist w_0 of the cavity mode and to maximize its finesse $\mathcal{F}$. To achieve this, it is necessary to optimize several geometrical characteristics simultaneously while complying with experimental requirements specific to each application. We now study the relationships between the geometrical characteristics of the concave structures, showing that they can be independently chosen to a larger extent than previously reported [47,48] by varying τ, w, and P_{CO_2}. We then point toward strategies to fabricate mirror templates tailored for two commonly used cavity geometries and their associated applications.

The relationship between the radius of curvature and the depth of the structures is shown in Figs. 5(a) and 5(b). It is most relevant to fiber-based cavity QED with solid-state emitters, or to other applications where an optical emitter is located on or near one of the mirrors. The optimal cavity geometry is the planar–concave geometry, for which the waist of the fundamental mode is given by $w_0^2 = \lambda L_{cav}/\pi\sqrt{1/\varepsilon - 1}$, with $\varepsilon = L_{cav}/\text{ROC} \in [0, 1]$. ROC is the radius of curvature of the concave mirror, and L_{cav} is the cavity length. It is usually
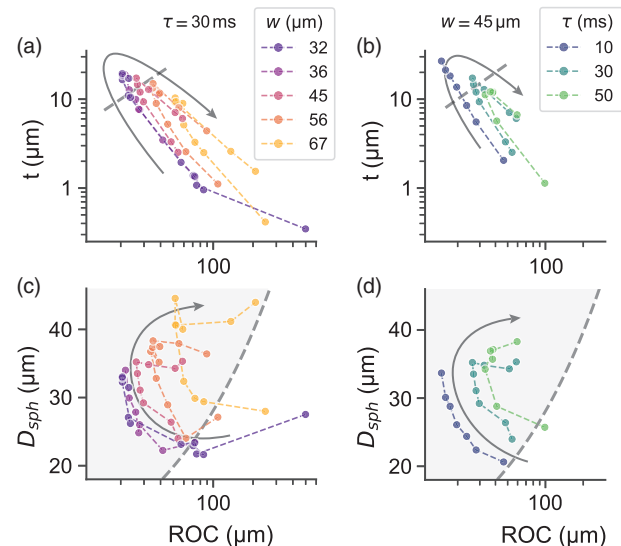

Fig. 5. Plots of the relationships between geometrical characteristics, with the direction of increasing pulse power shown by the gray arrows. (a), (b) Structure depth as a function of radius of curvature for various spot sizes and pulse durations, respectively. The dashed line follows $t = \text{ROC}/2$. (c), (d) Spherical diameter as a function of radius of curvature for various spot sizes and pulse durations, respectively. The shaded area shows the region where clipping losses are small in the case when $\varepsilon = 1$.

desirable to minimize both the cavity length and the radius of curvature in order to decrease the mode waist, the physical limit for L_{cav} being the depth of the structure. One should additionally make sure that $L_{cav} < ROC/2$ in order to prevent finesse deterioration due to diffraction losses [29]. A rough guideline for the best cavity geometry is then $L_{cav} = t = ROC/2$ [shown as a gray dashed line in Figs. 5(a) and 5(b)], with ROC and t as small as possible. The ablation results plotted in Figs. 5(a) and 5(b) show a strong nonlinear relationship between the radius of curvature and the depth of structures ablated with varying pulse power at constant spot size and pulse duration. However, we observe that this relationship depends strongly on the values of spot size and pulse duration. Structures with favorable geometries can be produced using short pulse durations, small spot sizes, and high pulse powers within regime 3. Smaller spot sizes can be achieved both by decreasing Δz and by using a focusing lens with a larger numerical aperture.

In contrast, another category of applications exists for which experimental constraints limit how short the cavity can be made. Fiber-based cavity QED with trapped atoms or ions, fiber-based cavity optomechanics, or other applications where the emitter or mechanical resonator is located in between the two mirrors belong to this category. The preferred cavity geometry is then the symmetric geometry. For these relatively long cavities, one of the main difficulties is to maintain a high finesse. Finesse is degraded by clipping losses, which arise when the spot size of the fundamental mode of the cavity on the end mirrors becomes large compared to the spherical diameter. The condition on D_{sph} for clipping losses not to significantly degrade the finesse of a symmetric cavity is given by [10] $D_{sph}^2 \geq \ln(5\mathcal{F}/\pi)\lambda L_{cav}/(\pi\sqrt{\varepsilon(2-\varepsilon)})$, with $\varepsilon \in [0, 2]$. In order to minimize waist while maintaining a high finesse, one should choose structures with the smallest radii possible that satisfy both the above condition and $ROC > L_{cav}$. The relationship between the spherical diameter and the radius of curvature of the structures is plotted in Figs. 5(c) and 5(d), with the small clipping losses region shown for $L_{cav} = ROC$. Craters fabricated with a high pulse power within regime 4 exhibit the largest spherical diameters, while pulse duration or spot size can be changed to adjust the radius of curvature.

5. CONCLUSION

In conclusion, we perform a systematic study of the effect of single-shot CO_2 laser ablation parameters on the geometry of fiber tips. We observe that ROC, t, and D_{out} exhibit extrema as a function of P_{CO_2} and τ (see Fig. 4). We speculate that these extrema arise from the combination of surface tension and boundary effects originating from the limited radial size of the fibers. Associated with this, we find that compound concave–convex shapes can be produced using a simple single-shot ablation procedure (regime 4 in Fig. 3). Such shapes are useful for small-mode-volume cavities and previously required tapering of the fiber in an additional processing step [43]. We further find that individually tuning the pulse power, pulse duration, and spot size extends the range of geometries that can be created. Based on these observations, we develop guidelines for the fabrication of fiber mirror templates optimized for experiments in

optomechanics and CQED. Finally, we expect that using shorter laser pulses and smaller spot sizes than presented here will enable to simultaneously decrease ROC and crater depth further.

REFERENCES

1. G. Staupendahl and P. Gerling, "Laser material processing of glasses with CO_2 lasers," Proc. SPIE **3097**, 670–677 (1997).
2. C. Weingarten, E. Uluz, A. Schmickler, K. Braun, E. Willenborg, A. Temmler, and S. Heidrich, "Glass processing with pulsed CO_2 laser radiation," Appl. Opt. **56**, 777–783 (2017).
3. L. Collot, V. Lefèvre-Seguin, M. Brune, J. M. Raimond, and S. Haroche, "Very high-Q whispering-gallery mode resonances observed on fused silica microspheres," Europhys. Lett. **23**, 327 (1993).
4. U. C. Paek and A. L. Weaver, "Formation of a spherical lens at optical fiber ends with a CO_2 Laser," Appl. Opt. **14**, 294–298 (1975).
5. M. Wakaki, Y. Komachi, and G. Kanai, "Microlenses and microlens arrays formed on a glass plate by use of a CO_2 laser," Appl. Opt. **37**, 627–631 (1998).
6. D. K. Armani, T. J. Kippenberg, S. M. Spillane, and K. J. Vahala, "Ultra-high-Q toroid microcavity on a chip," Nature **421**, 925–928 (2003).
7. K. L. Wlodarczyk, N. J. Weston, M. Ardron, and D. P. Hand, "Direct CO_2 laser-based generation of holographic structures on the surface of glass," Opt. Express **24**, 1447 (2016).
8. D. Hunger, C. Deutsch, R. J. Barbour, R. J. Warburton, and J. Reichel, "Laser micro-fabrication of concave, low-roughness features in silica," AIP Adv. **2**, 012119 (2012).
9. B. Petrak, K. Konthasinghe, S. Perez, and A. Muller, "Feedback-controlled laser fabrication of micromirror substrates," Rev. Sci. Instrum. **82**, 123112 (2011).
10. D. Hunger, T. Steinmetz, Y. Colombe, C. Deutsch, T. W. Hänsch, and J. Reichel, "A fiber Fabry-Perot cavity with high finesse," New J. Phys. **12**, 065038 (2010).
11. A. Muller, E. B. Flagg, J. R. Lawall, and G. S. Solomon, "Ultrahigh-finesse, low-mode-volume Fabry-Perot microcavity," Opt. Lett. **35**, 2293–2295 (2010).
12. Y. Colombe, T. Steinmetz, G. Dubois, F. Linke, D. Hunger, and J. Reichel, "Strong atom-field coupling for Bose-Einstein condensates in an optical cavity on a chip," Nature **450**, 272–276 (2007).
13. A. Muller, E. B. Flagg, M. Metcalfe, J. Lawall, and G. S. Solomon, "Coupling an epitaxial quantum dot to a fiber-based external-mirror microcavity," Appl. Phys. Lett. **95**, 173101 (2009).
14. C. Toninelli, Y. Delley, T. Störferle, A. Renn, S. Götzinger, and V. Sandoghdar, "A scanning microcavity for in situ control of single-molecule emission," Appl. Phys. Lett. **97**, 021107 (2010).
15. M. Steiner, H. M. Meyer, C. Deutsch, J. Reichel, and M. Köhl, "Single ion coupled to an optical fiber cavity," Phys. Rev. Lett. **110**, 043003 (2013).
16. J. Miguel-Sánchez, A. Reinhard, E. Togan, T. Volz, A. Imamoglu, B. Besga, J. Reichel, and J. Estève, "Cavity quantum electrodynamics

with charge-controlled quantum dots coupled to a fiber Fabry-Perot cavity," New J. Phys. **15**, 045002 (2013).

17. R. Albrecht, A. Bommer, C. Deutsch, J. Reichel, and C. Becher, "Coupling of a single nitrogen-vacancy center in diamond to a fiber-based microcavity," Phys. Rev. Lett. **110**, 243602 (2013).

18. B. Brandstätter, A. McClung, K. Schüppert, B. Casabone, K. Friebe, A. Stute, P. O. Schmidt, C. Deutsch, J. Reichel, R. Blatt, and T. E. Northup, "Integrated fiber-mirror ion trap for strong ion-cavity coupling," Rev. Sci. Instrum. **84**, 123104 (2013).

19. B. Besga, C. Vaneph, J. Reichel, J. Estève, A. Reinhard, J. Miguel-Sánchez, A. Imamoğlu, and T. Volz, "Polariton boxes in a tunable fiber cavity," Phys. Rev. Appl. **3**, 014008 (2015).

20. I. Favero, S. Stapfner, D. Hunger, P. Paulitschke, J. Reichel, H. Lorenz, E. M. Weig, and K. Karrai, "Fluctuating nanomechanical system in a high finesse optical microcavity," Opt. Express **17**, 12813–12820 (2009).

21. N. E. Flowers-Jacobs, S. W. Hoch, J. C. Sankey, A. Kashkanova, A. M. Jayich, C. Deutsch, J. Reichel, and J. G. E. Harris, "Fiber-cavity-based optomechanical device," Appl. Phys. Lett. **101**, 221109 (2012).

22. S. Stapfner, L. Ost, D. Hunger, J. Reichel, I. Favero, and E. M. Weig, "Cavity-enhanced optical detection of carbon nanotube Brownian motion," Appl. Phys. Lett. **102**, 151910 (2013).

23. H. Zhong, G. Fläschner, A. Schwarz, R. Wiesendanger, P. Christoph, T. Wagner, A. Bick, C. Staarmann, B. Abeln, K. Sengstock, and C. Becker, "A millikelvin all-fiber cavity optomechanical apparatus for merging with ultra-cold atoms in a hybrid quantum system," Rev. Sci. Instrum. **88**, 023115 (2017).

24. H. Takahashi, J. Morphew, F. Oručević, A. Noguchi, E. Kassa, and M. Keller, "Novel laser machining of optical fibers for long cavities with low birefringence," Opt. Express **22**, 31317–31328 (2014).

25. K. Ott, S. Garcia, R. Kohlhaas, K. Schüppert, P. Rosenbusch, R. Long, and J. Reichel, "Millimeter-long fiber Fabry-Perot cavities," Opt. Express **24**, 9839 (2016).

26. S. Garcia, F. Ferri, K. Ott, J. Reichel, and R. Long, "Dual-wavelength fiber Fabry-Perot cavities with engineered birefringence," Opt. Express **26**, 22249–22263 (2018).

27. J.-M. Cui, K. Zhou, M.-S. Zhao, M.-Z. Ai, C.-K. Hu, Q. Li, B.-H. Liu, J.-L. Peng, Y.-F. Huang, C.-F. Li, and G.-C. Guo, "Polarization non-degenerate fiber Fabry-Perot cavities with large tunable splittings," Appl. Phys. Lett. **112**, 171105 (2018).

28. J. Gallego, S. Ghosh, S. K. Alavi, W. Alt, M. Martinez-Dorantes, D. Meschede, and L. Ratschbacher, "High-finesse fiber Fabry-Perot cavities: stabilization and mode matching analysis," Appl. Phys. B **122**, 1–14 (2016).

29. J. Benedikter, T. Hümmer, M. Mader, B. Schlederer, J. Reichel, T. W. Hänsch, and D. Hunger, "Transverse-mode coupling and diffraction loss in tunable Fabry-Pérot microcavities," New J. Phys. **17**, 053051 (2015).

30. A. Bick, C. Staarmann, P. Christoph, O. Hellmig, J. Heinze, K. Sengstock, and C. Becker, "The role of mode match in fiber cavities," Rev. Sci. Instrum. **87**, 013102 (2016).

31. N. Podoliak, H. Takahashi, M. Keller, and P. Horak, "Harnessing the mode mixing in optical fiber-tip cavities," J. Phys. B **50**, 085503 (2017).

32. M. Uphoff, M. Brekenfeld, G. Rempe, and S. Ritter, "Frequency splitting of polarization eigenmodes in microscopic Fabry-Perot cavities," New J. Phys. **17**, 013053 (2015).

33. H. Takahashi, E. Kassa, C. Christoforou, and M. Keller, "Strong coupling of a single ion to an optical cavity," arXiv:1808.04031 (2018).

34. J. Gallego, W. Alt, T. Macha, M. Martinez-Dorantes, D. Pandey, and D. Meschede, "Strong Purcell effect on a neutral atom trapped in an open fiber cavity," Phys. Rev. Lett. **121**, 173603 (2018).

35. J. Benedikter, H. Kaupp, T. Hümmer, Y. Liang, A. Bommer, C. Becher, A. Krueger, J. M. Smith, T. W. Hänsch, and D. Hunger, "Cavity-enhanced single-photon source based on the silicon-vacancy center in diamond," Phys. Rev. Appl. **7**, 024031 (2017).

36. A. B. Shkarin, A. D. Kashkanova, C. D. Brown, S. Garcia, K. Ott, J. Reichel, and J. G. E. Harris, "Quantum optomechanics in a liquid," Phys. Rev. Lett. **122**,153601 (2019).

37. T. Doualle, L. Gallais, P. Cormont, D. Hébert, P. Combis, and J.-L. Rullier, "Thermo-mechanical simulations of CO_2 laser-fused silica interactions," J. Appl. Phys. **119**, 113106 (2016).

38. E. Mendez, K. M. Nowak, H. J. Baker, F. J. Villarreal, and D. R. Hall, "Localized CO_2 laser damage repair of fused silica optics," Appl. Opt. **45**, 5358–5367 (2006).

39. G. A. J. Markillie, H. J. Baker, F. J. Villarreal, and D. R. Hall, "Effect of vaporization and melt ejection on laser machining of silica glass micro-optical components," Appl. Opt. **41**, 5660–5667 (2002).

40. T. He, C. Wei, Z. Jiang, Z. Yu, Z. Cao, and J. Shao, "Numerical model and experimental demonstration of high precision ablation of pulse CO_2 laser," Chin. Opt. Lett. **16**, 41401 (2018).

41. M. D. Feit and A. M. Rubenchik, "Mechanisms of CO_2 laser mitigation of laser damage growth in fused silica," Proc. SPIE **4932**, 91–103 (2003).

42. K. M. Nowak, H. J. Baker, and D. R. Hall, "Analytical model for CO_2 laser ablation of fused quartz," Appl. Opt. **54**, 8653 (2015).

43. H. Kaupp, T. Hümmer, M. Mader, B. Schlederer, J. Benedikter, P. Haeusser, H.-C. Chang, H. Fedder, T. W. Hänsch, and D. Hunger, "Purcell-enhanced single-photon emission from nitrogen-vacancy centers coupled to a tunable microcavity," Phys. Rev. Appl. **6**, 054010 (2016).

44. M. Mader, J. Reichel, T. W. Hänsch, and D. Hunger, "A scanning cavity microscope," Nat. Commun. **6**, 7249 (2015).

45. B. Petrak, N. Djeu, and A. Muller, "Purcell-enhanced Raman scattering from atmospheric gases in a high-finesse microcavity," Phys. Rev. A **89**, 023811 (2014).

46. T. Hümmer, J. Noe, M. S. Hofmann, T. W. Hänsch, A. Högele, and D. Hunger, "Cavity-enhanced Raman microscopy of individual carbon nanotubes," Nat. Commun. **7**, 12155 (2016).

47. L. Greuter, S. Starosielec, D. Najer, A. Ludwig, L. Duempelmann, D. Rohner, and R. J. Warburton, "A small mode volume tunable microcavity: development and characterization," Appl. Phys. Lett. **105**, 121105 (2014).

48. D. Najer, M. Renggli, D. Riedel, S. Starosielec, and R. J. Warburton, "Fabrication of mirror templates in silica with micron-sized radii of curvature," Appl. Phys. Lett. **110**, 011101 (2017).